

Supplementary materials for

Seismically anisotropic magma reservoirs underlying silicic super-eruptions

Chengxin Jiang¹, Brandon Schmandt¹, Jamie Farrell², Fan-Chi Lin², Kevin M. Ward²

1. Department of Earth and Planetary Sciences, The University of New Mexico, Albuquerque, NM 87131

2. Department of Geology and Geophysics, The University of Utah, Salt Lake City, UT 84112

This file includes:

Materials on ambient noise surface wave tomography

Tables DR1 to DR2

Figures DR1 to DR10 and associated figure captions

References

Ambient noise surface wave tomography

In this study, we used about two years of continuous recordings from the seismic stations shown in Fig. 1. Data from all three components were used for the networks listed in Table S1, except for the NC, where only vertical-component data are available. Pre-processing of the continuous noise data before cross-correlation is performed on the daily component of E, N and Z respectively, by following Bensen et al., (2007) and Lin et al., (2008). This includes removing the mean, trend and instrument response, and bandpass filtering between 2 and 100 s periods. The daily cross-correlations were performed between the vertical–vertical (Z-Z), north–north (N-N), north–east (N-E), east–east (E-E) and east–north (E-N) components and stacked into one time-series for each station-pair. Then the cross-correlations of the five components were rotated to achieve transverse–transverse (T-T), transverse–radial (T-R), radial–radial (R-R) and radial–transverse (R-T) cross-correlations following equation 1 of Lin et al. (2008). Finally, the vertical–vertical component cross-correlations were taken as the empirical Green’s functions for Rayleigh waves; whereas the transverse-transverse component cross-correlations were used for Love waves (Fig. S1).

We adopted the frequency-time analysis method (FTAN; Levshin et al., 2011) to measure the inter-station phase velocities for both Rayleigh and Love waves between all station-pairs. To ensure that only reliable measurements of phase velocities are used for tomography, quality control is performed with the selection based on two criteria: 1) the interstation distance must be larger than two wavelengths and 2) the Signal-to-Noise ratio (SNR) as defined in Bensen et al., (2007) must be larger than 6. All of the selected interstation phase measurements are implemented into a fast-marching-based ray tracing method (Rawlinson and Sambridge, 2003), which accounts for off-great circle propagation effects, to invert for isotropic phase velocity maps on a $0.1^{\circ} \times 0.1^{\circ}$ geographic grid for Long Valley and a $0.2^{\circ} \times 0.2^{\circ}$ geographic grid for Yellowstone. The phase

velocity maps constrain lateral variations for a given period. Phase velocities for all periods at each map location were then used to invert for V_s as a function of depth as described in the main text. This conventional two-step approach to surface wave dispersion tomography is described in greater detail in prior studies such as Xie et al. (2013).

In this study, we used the Computer Programs in Seismology (CPS; Herrmann 2013) to calculate dispersion curves for Monte Carlo search, rather than the code of MINOES (Masters et al., 2007; as used in Moschetti et al., 2010 and Guo et al., 2016) that more accurately models a transversely isotropic medium. This preference is mostly considering that CPS is much more computationally efficient while ensuring enough accuracy for the purpose of this study. Our synthetic tests, summarized in Fig. S4, validate the usage of CPS for the purpose of this study by showing that 1) the differences in the predicted dispersion curves from CPS and MINOES are much smaller compared to the phase velocity uncertainties, and 2) the resulted isotropic and anisotropic profiles from Markov Chain Monte Carlo inversion scheme implemented with CPS and MINOES are comparable to each other. Our synthetic test also shows that CPS is more than 2 orders of magnitude efficient (~ 1 hour for the inversion of 1 grid point) compared to MINOES (~ 200 hours for the same grid point).

Table DR1. Summary of seismic networks used in this study.

Seismic network	Study region	DOI
TA	Yellowstone & Long Valley	https://doi.org/10.7914/SN/TA
NC	Long Valley	https://doi.org/10.7914/SN/NC
XE	Long Valley	https://doi.org/10.7914/SN/XE_2005
XJ	Long Valley	https://doi.org/10.7914/SN/XJ_1997
CI	Long Valley	https://doi.org/10.7914/SN/CI
WY	Yellowstone	https://doi.org/10.7914/SN/WY
Z2	Yellowstone	Seats and Lawrence, 2014
PB	Yellowstone	Hasting et al., 2006
IW	Yellowstone	https://doi.org/10.7914/SN/IW
US	Yellowstone	https://doi.org/10.7914/SN/US

Table DR2. Tomography model space for each model variable at both study areas

Model variable	Model space for Long Valley	Model space for Yellowstone
1st B-spline coefficients of crust (V_{SV} and V_{SH})	2.0 km/s – 3.5 km/s	2.0 km/s – 3.5 km/s
2nd B-spline coefficients of crust (V_{SV} and V_{SH})	2.5 km/s – 3.8 km/s	2.0 km/s – 3.8 km/s
3rd B-spline coefficients of crust (V_{SV} and V_{SH})	2.8 km/s – 3.8 km/s	2.5 km/s – 3.8 km/s
4th B-spline coefficients of crust (V_{SV} and V_{SH})	2.8 km/s – 4.0 km/s	2.8 km/s – 4.0 km/s
5th B-spline coefficients of crust (V_{SV} and V_{SH})	3.0 km/s – 4.2 km/s	3.0 km/s – 4.0 km/s
Mantle layer (V_{SV} and V_{SH})	4.0 km/s – 4.7 km/s	4.0 km/s – 4.7 km/s
Anisotropy at all depths	-20% – 20%	-20% – 20%

Figure DR1. Cross-correlations for three stations close to the Long Valley caldera (XE-SNP36, XE-SNP45 and XE-SNP46) with the rest stations as a function of inter-station distance.

Waveforms of Rayleigh (from Z-Z component) and Love wave (from T-T component) were filtered at two frequency bands of 0.09-0.15 Hz and 0.035-0.06 Hz, respectively. The thick dashed yellow lines delineate the approximate arrival times for surface wave velocity of 2.5 km/s in A, 3.0 km/s in B, 3.33 km/s in C and 4 km/s in D. Note that these waveforms are resulted from the quality control procedure detailed in the “ambient noise surface wave tomography” of the supplementary material.

Figure DR2. Resolution analysis for the phase velocity maps at 10 and 20 s for Long Valley and Yellowstone, respectively. The horizontal resolution length-scale of our tomography is ~20 km for Long Valley and ~30 km for Yellowstone.

Figure DR3. Phase velocity maps of the Rayleigh and Love waves derived from the ambient noise tomography. (A-C) Rayleigh wave phase velocity maps at Long Valley caldera. (D-F) Love wave phase velocity maps at Long Valley Caldera. (G-I) Rayleigh wave phase velocity maps at Yellowstone. (J-L) Love wave phase velocity maps at Yellowstone. The regional average of each map is marked at the bottom left of each figure. The phase velocity inversion is performed on a $0.1^\circ \times 0.1^\circ$ grid for Long Valley and $0.2^\circ \times 0.2^\circ$ grid for Yellowstone, respectively.

Figure DR4. Synthetic tests to validate the usage of the CPS package for this study by comparing with the results from Minos (Masters et al., 2007). The synthetic tests include forward modelling of predicted dispersion curves from the same isotropic (A) and anisotropic model (B), and

inversion results of V_{SV} , V_{SH} (C) and anisotropic structures (D) using the same dispersion data from a real example beneath the Long Valley caldera (-118.8° , 37.6°). The inversion results shown in Fig. S4C-4D are both from the Markov chain Monte Carlo inversion scheme with the implementation of CPS and Minos packages for the forward calculations, respectively.

Figure DR5. Examples of surface-wave dispersion fitting from inversions with only isotropic parameters (A, C) and anisotropic parameters (B, D) at two grid points within the calderas. The black curves with 1-sigma error bars are our observations, and the blue and red curves are the predicted Rayleigh and Love wave dispersion curves by the 800 best-fitting models. The number on the lower right of each subfigure denotes the chi-squared misfit of the best-fitting model. During the inversion, the model space is a set of 1-D shear velocity profiles composed of crust and uppermost mantle domains. The crust is parameterized by 5 B-spline coefficients and the uppermost mantle is composed of a layer from the local Moho (fixed according to Schmandt et al., 2015) to 60 km depth overlying a half-space with the same physical properties. The V_p and density are scaled to V_s following Jiang et al., (2018).

Figure DR6. Misfit to surface-wave dispersion data in the study regions of Long Valley caldera (A-D) and Yellowstone (E-H). The column on the left shows the chi-squared misfit from the first step inversion by assuming an isotropic model; whereas the column on the right is for the second step inversion where anisotropic parameters are introduced. Note that the upper panel for each study region represent the misfit from the best-fitting model, whereas the lower panel is from the average of the 800 best-fitting models.

Figure DR7. The effects of applying different culling criteria on the resulted anisotropic structures averaged at different depths in Long Valley caldera. Each column represents the results of retaining the anisotropic structures without applying any culling and with different culling criteria of where zero is at least 1-sigma, 1.5-sigma and 2-sigma away from the mean anisotropy based on the 800 selected models from the Markov chain Monte Carlo inversion.

Figure DR8. Same as Fig. S7, but for Yellowstone.

Figure DR9. Synthetic tests to demonstrate the resolvability of our inversion scheme on the depth-dependent anisotropy. The synthetic tests used the average phase velocity uncertainties, which were similar for both study areas (30–60 m/s), so the results are relevant regarding resolution of deep crustal anisotropy beneath both calderas. The inversion scheme is able to distinguish between the positive anisotropy only confined at 5-18 km depth (A) and the same amplitude anisotropy extending from 5 km through the entire crustal column (B). However, it could not resolved $\leq 2.5\%$ anisotropy from 18 km to the Moho with anisotropy at 5-18 km depth same to those in A and B. The additional test in D shows that the inversion scheme is also able to resolve lower crustal anisotropy (at least with the 68% confidence) if it exists, even though the real amplitude is probably underestimated due to the trade-off to the shallow crust anisotropy. The dashed black lines are the input anisotropic structures, and the blue lines represent the mean anisotropy based on the 800 selected models from the Markov chain Monte Carlo inversion along with the estimated 1 standard deviation. The green lines denote zero anisotropy, and the dashed grey lines represent the 38 km deep Moho discontinuity, which is fixed in the inversion.

Figure DR10. Isotropic Vs and anisotropic maps averaged at 0-5 km depth beneath and around the (A-B) Long Valley and (C-D) Yellowstone.

References

- Bensen, G.D., Ritzwoller, M.H., Barmin, M.P., Levshin, A.L., Lin, F., Moschetti, M.P., Shapiro, N.M. and Yang, Y., 2007, Processing seismic ambient noise data to obtain reliable broadband surface wave dispersion measurements: *Geophysical Journal International*, v. 169, p. 1239-1260.
- Guo, Z., Yang, Y. and Chen, Y.J., 2016. Crustal radial anisotropy in Northeast China and its implications for the regional tectonic extension. *Geophysical Journal International*, v. 207, p.197-208.
- Hasting, M., Eakins, J., Anderson, G., Hodgkinson, K., Johnson, W., Mencin, D., Smith, S., Jackson, M. and Prescott, W., 2006, The Plate Boundary Observatory Borehole Seismic Network. Abstract G53B-0901 at 2006 AGU Fall Meeting, AGU, San Francisco, California, 11-15 December.
- Herrmann, R.B., 2013, Computer programs in seismology: An evolving tool for instruction and research: *Seismological Research Letters*, v. 84, p. 1081-1088.
- Jiang, C., Schmandt, B., Hansen, S.M., Dougherty, S.L., Clayton, R.W., Farrell, J. and Lin, F.C., 2018, Rayleigh and S wave tomography constraints on subduction termination and lithospheric foundering in central California: *Earth and Planetary Science Letters*, v. 488, p. 14-26.
- Levshin, A.L. and Ritzwoller, M.H., 2001. Automated detection, extraction, and measurement of regional surface waves. In *Monitoring the Comprehensive Nuclear-Test-Ban Treaty: Surface Waves* (p. 1531-1545). Birkhäuser, Basel.
- Lin, F.C., Moschetti, M.P. and Ritzwoller, M.H., 2008. Surface wave tomography of the western United States from ambient seismic noise: Rayleigh and Love wave phase velocity maps. *Geophysical Journal International*, v. 173, p. 281-298.
- Masters, G., Barmine, M.P. and Kientz, S., 2007, Mineos User's Manual, in *Computational Infrastructure for Geodynamics*, California Institute of Technology, Pasadena.

- Moschetti, M.P., Ritzwoller, M.H., Lin, F. and Yang, Y., 2010, Seismic evidence for widespread western-US deep-crustal deformation caused by extension: *Nature*, v. 464, p. 885-889.
- Rawlinson, N. and Sambridge, M., 2003, Seismic traveltime tomography of the crust and lithosphere: *Advances in Geophysics*, v. 46, p. 81-199.
- Schmandt, B., Lin, F.C. and Karlstrom, K.E., 2015, Distinct crustal isostasy trends east and west of the Rocky Mountain Front: *Geophysical Research Letters*, v. 42, no. 23, doi: 10.1002/2015GL066593.
- Seas, K.J. and Lawrence, J.F., 2014. The seismic structure beneath the Yellowstone Volcano Field from ambient seismic noise. *Geophysical Research Letters*, v. 41, p. 8277-8282.
- Xie, J., Ritzwoller, M. H., Shen, W., Yang, Y., Zheng, Y., and Zhou, L. 2013. Crustal radial anisotropy across eastern Tibet and the western Yangtze craton. *Journal of Geophysical Research: Solid Earth*, v. 118, p. 4226-4252.

Figure DR1

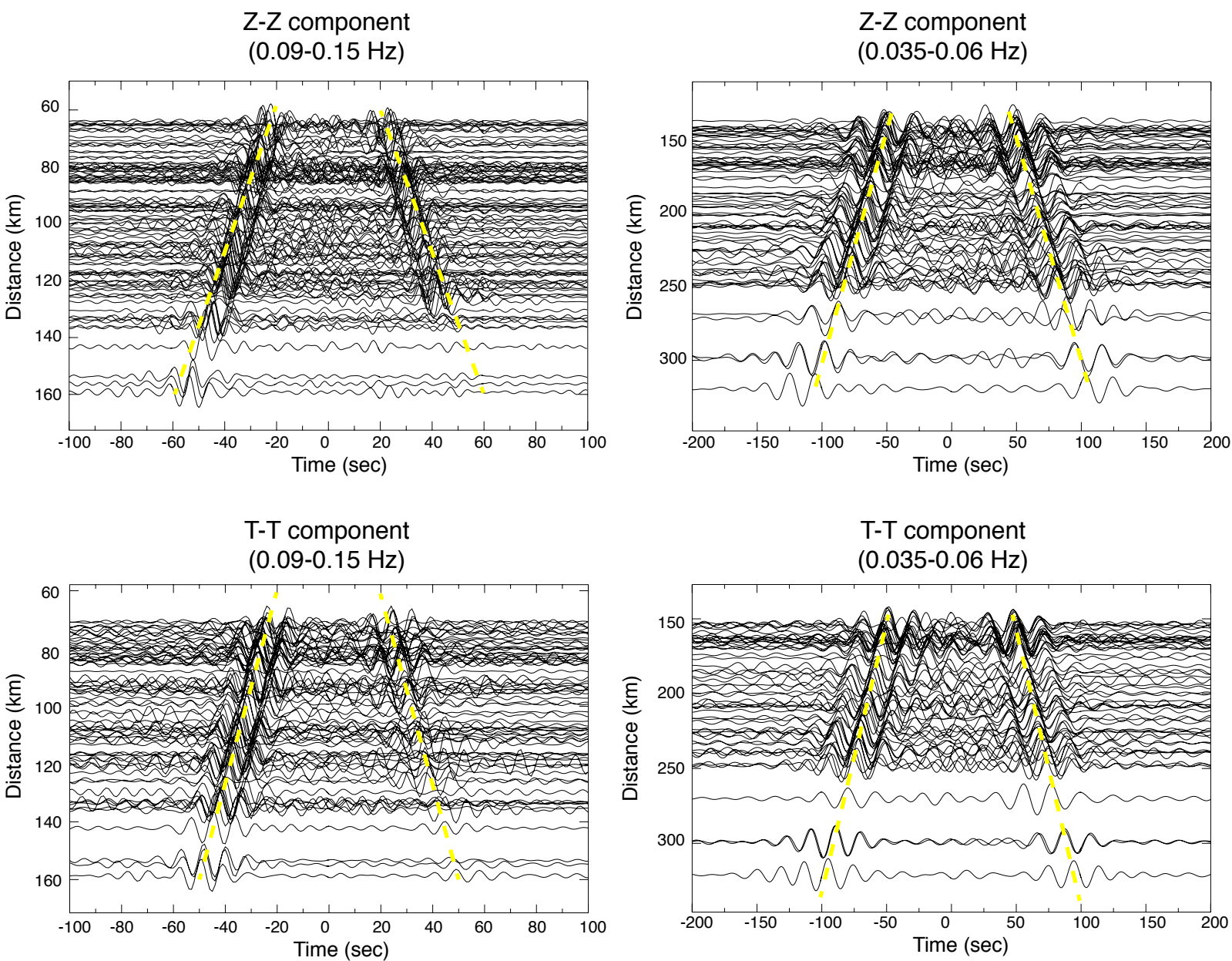


Figure DR2

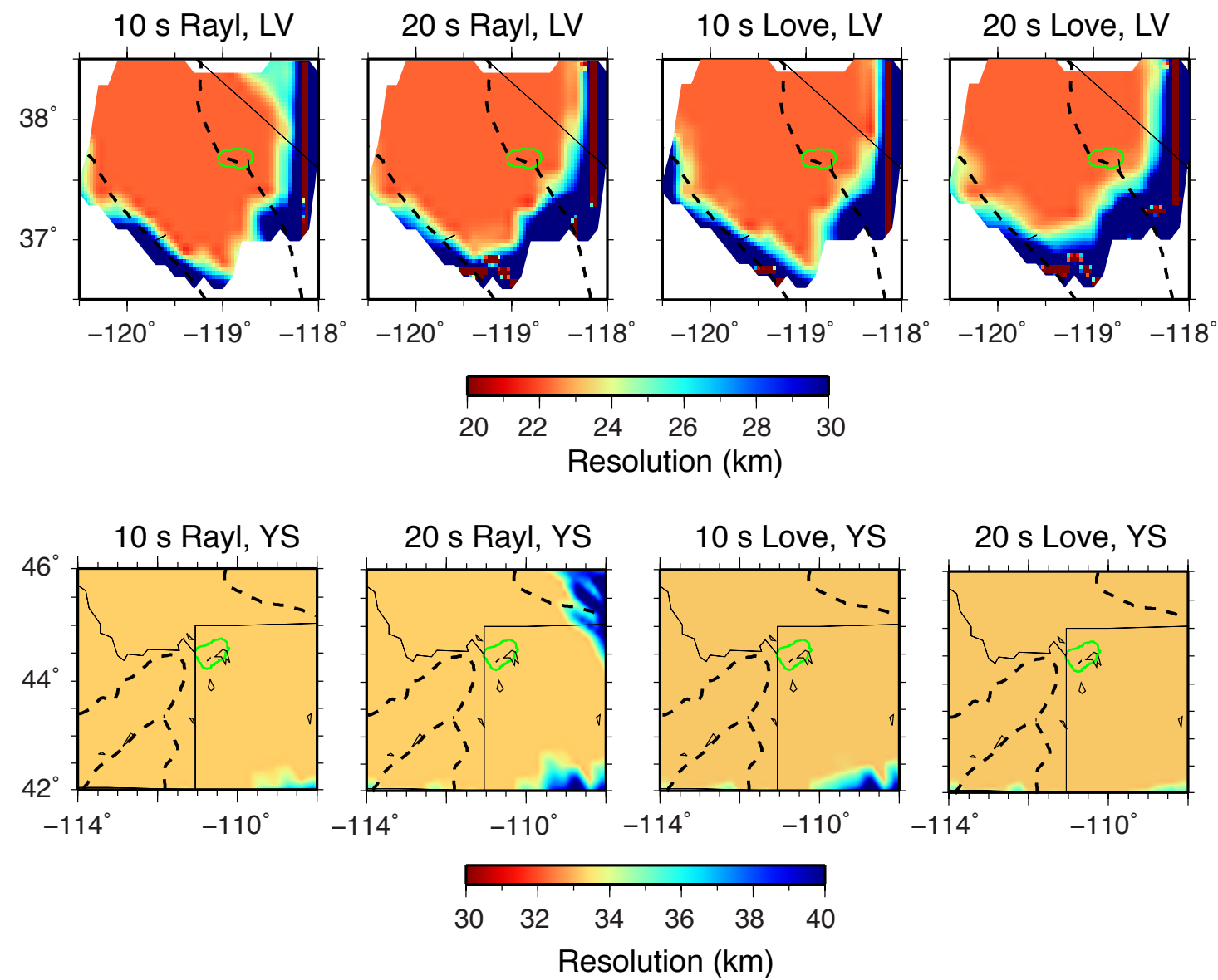
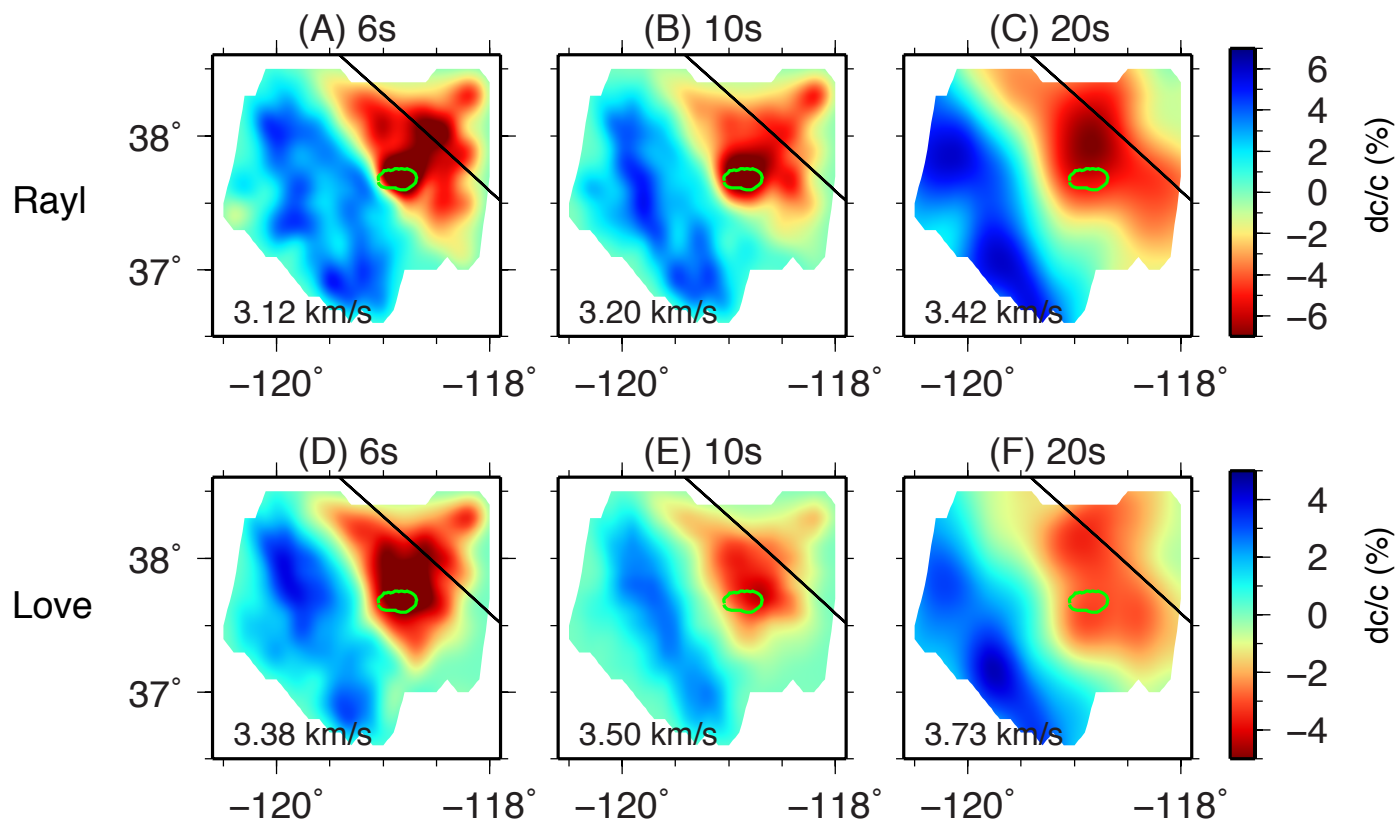


Figure DR3

Long Valley Caldera



Yellowstone

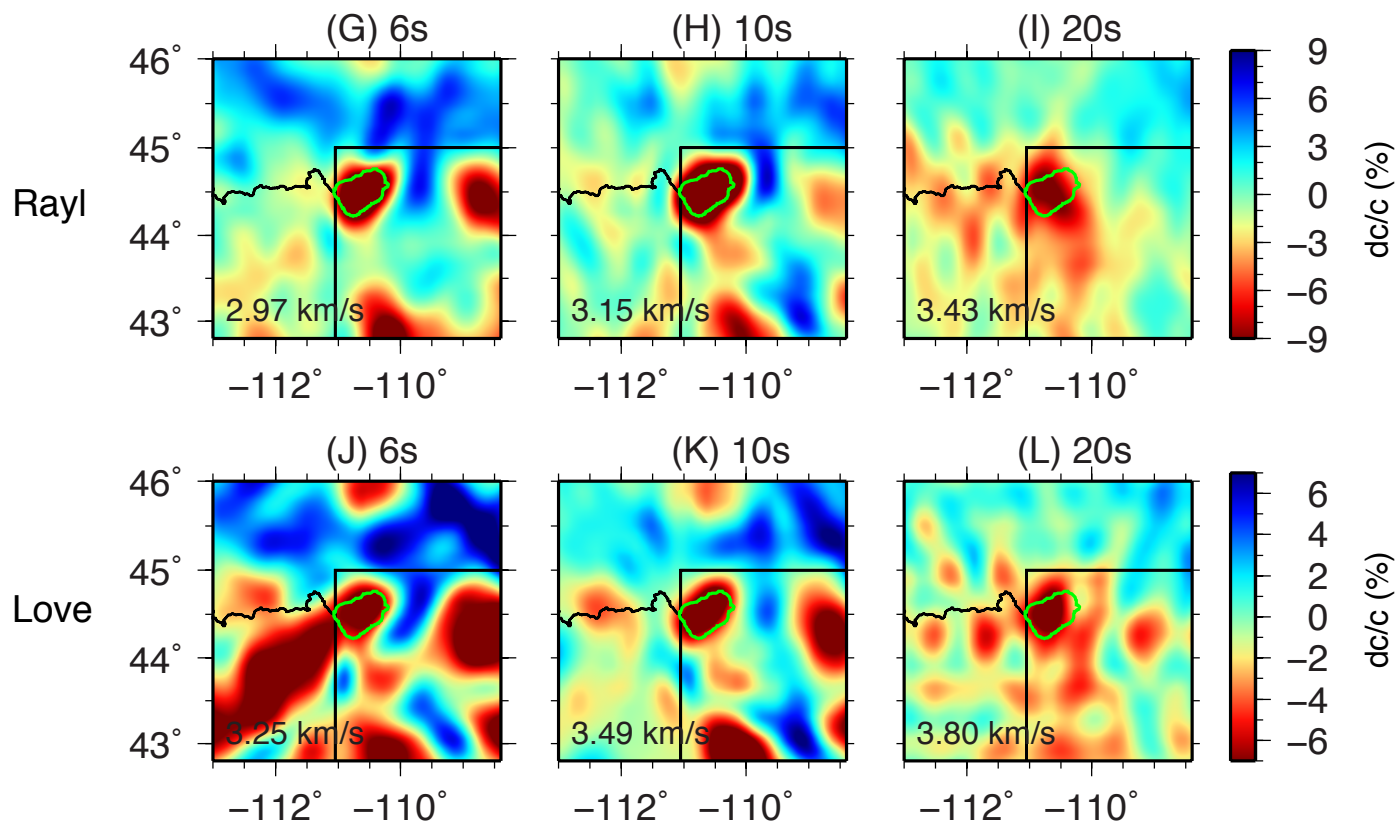


Figure DR4

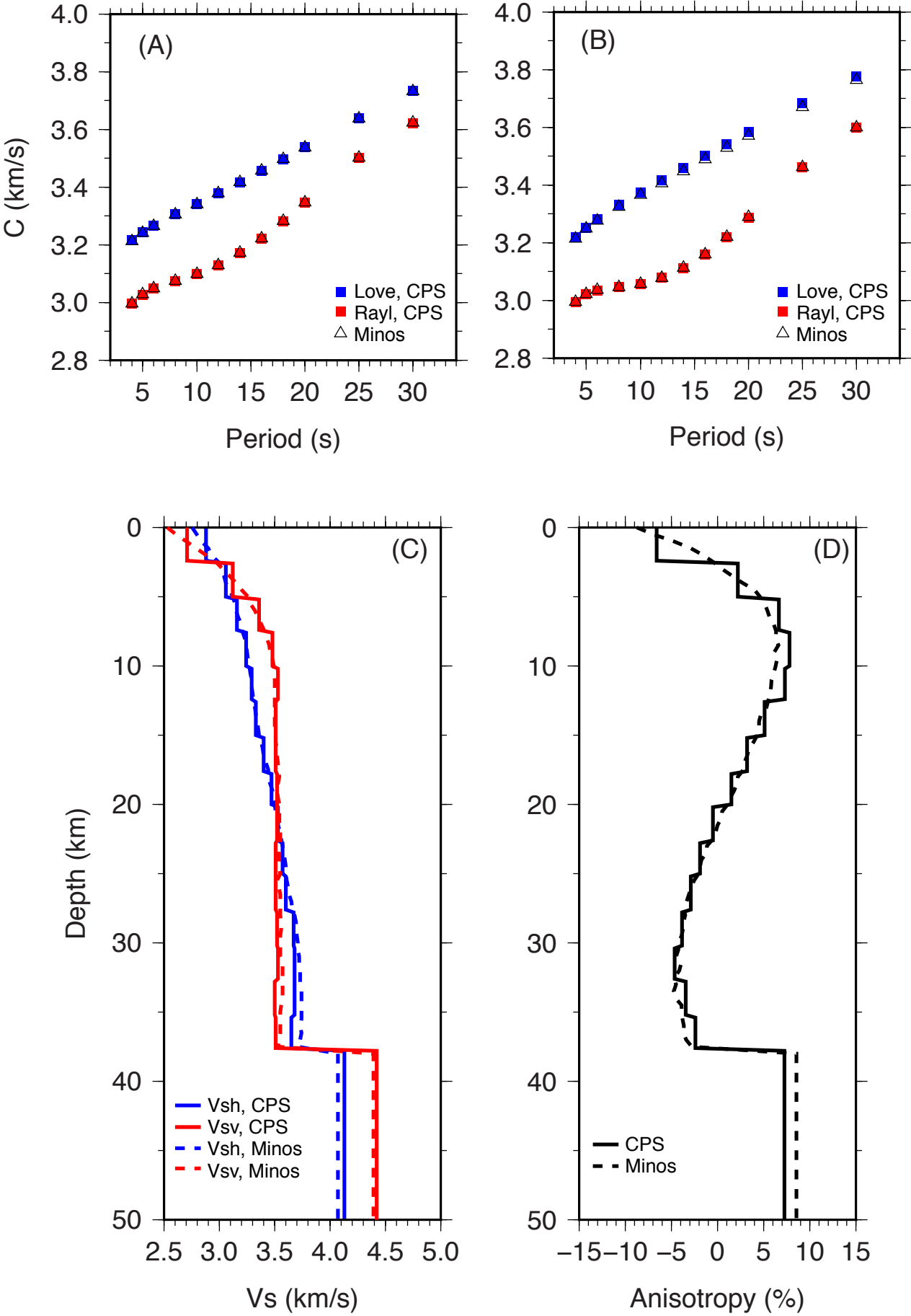
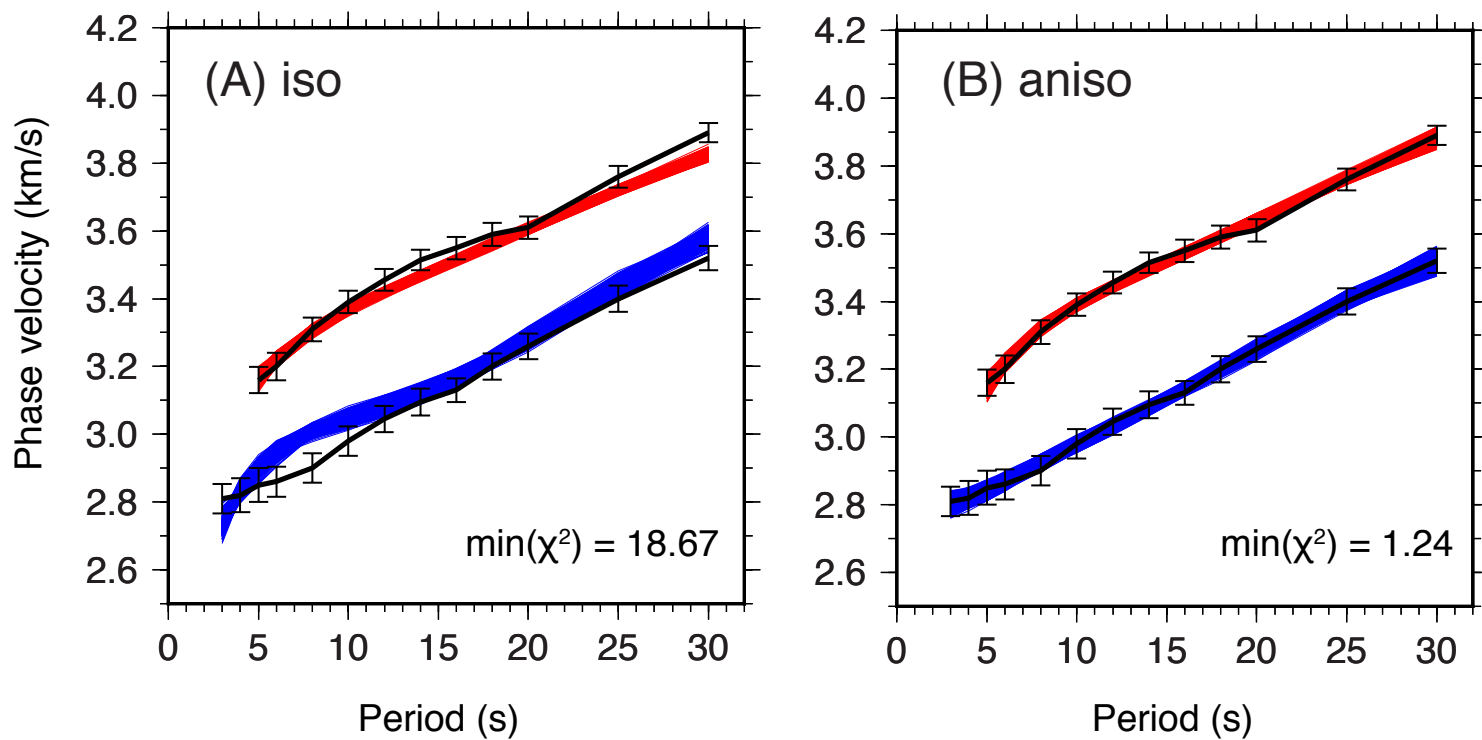


Figure DR5

**Long Valley Caldera
(-118.8° 37.6°)**



**Yellowstone
(-110.6° 44.4°)**

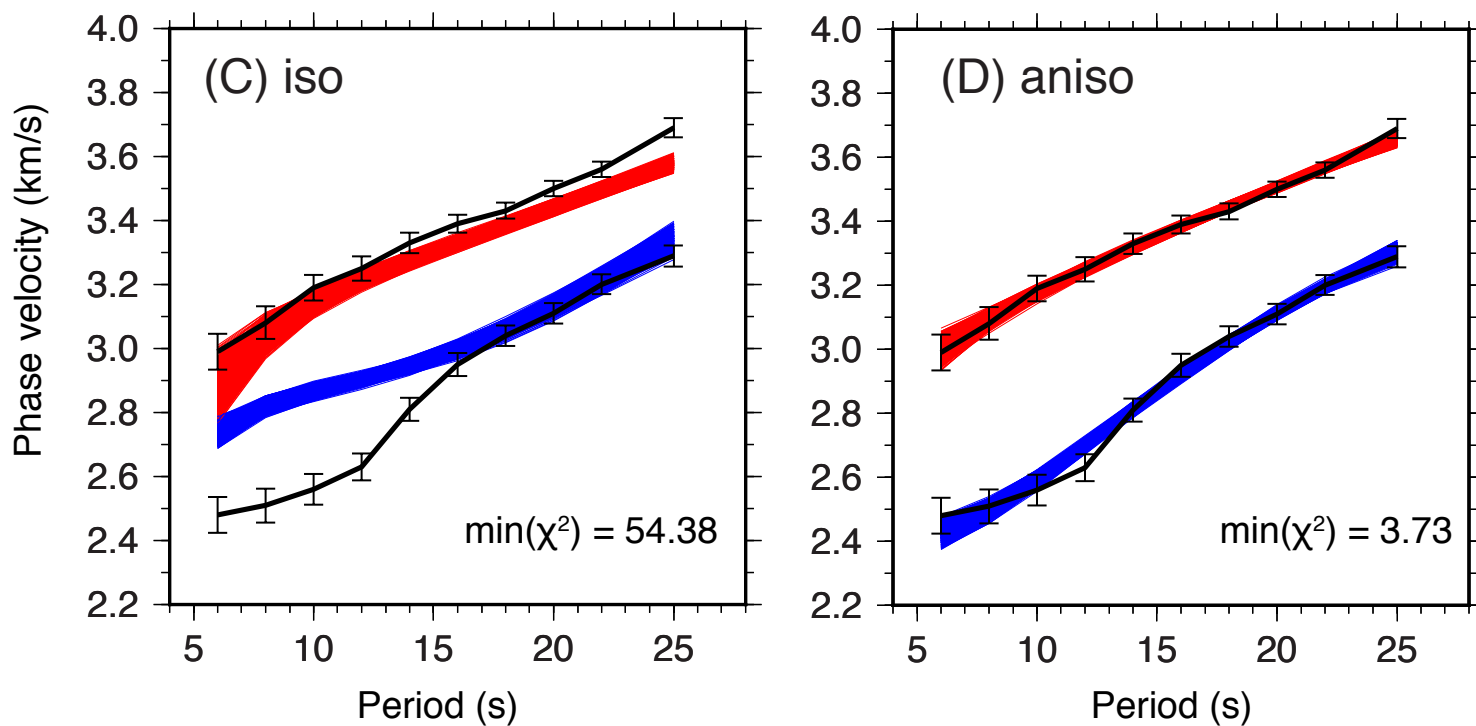
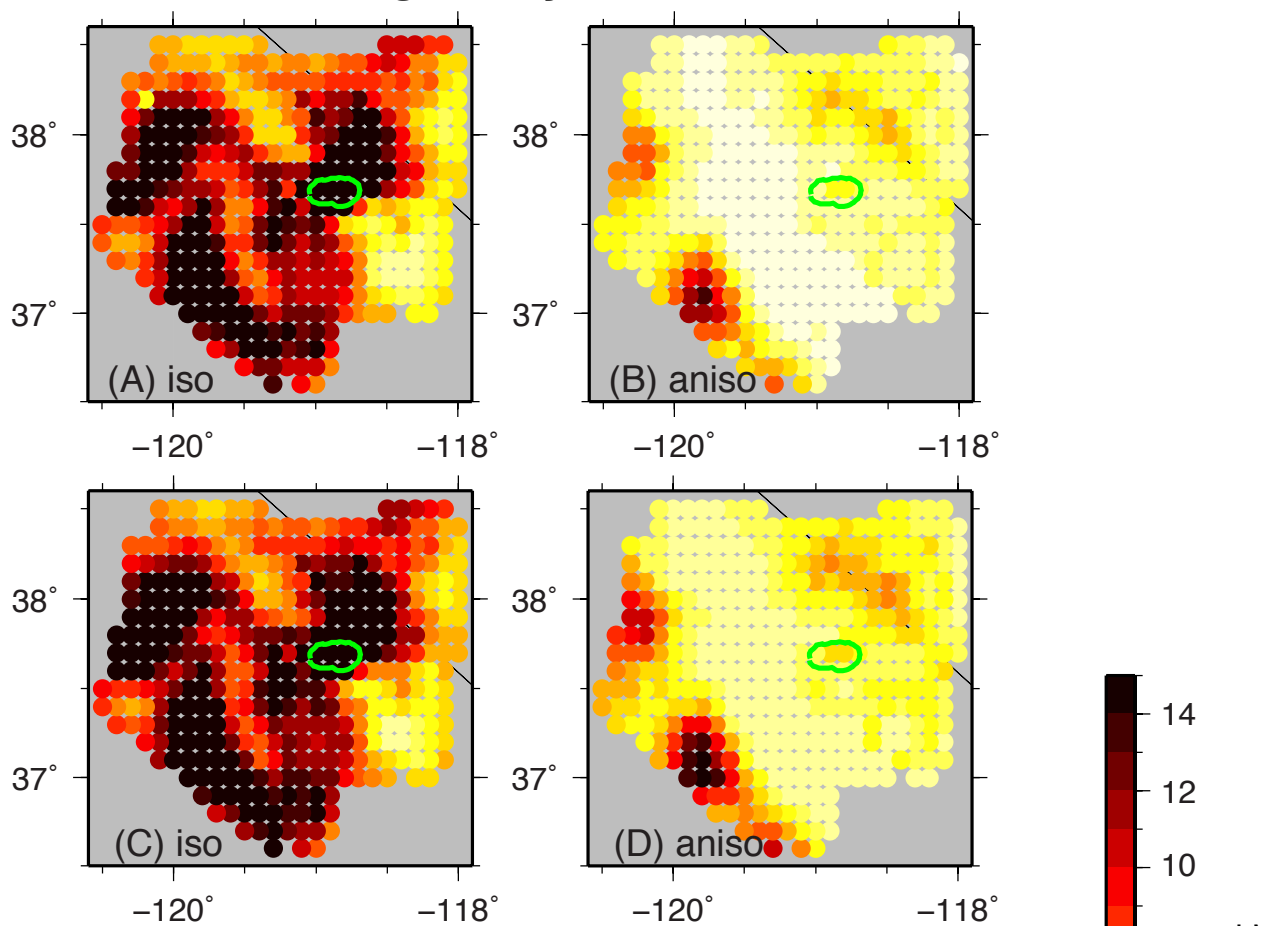


Figure DR6

Long Valley Caldera



Yellowstone

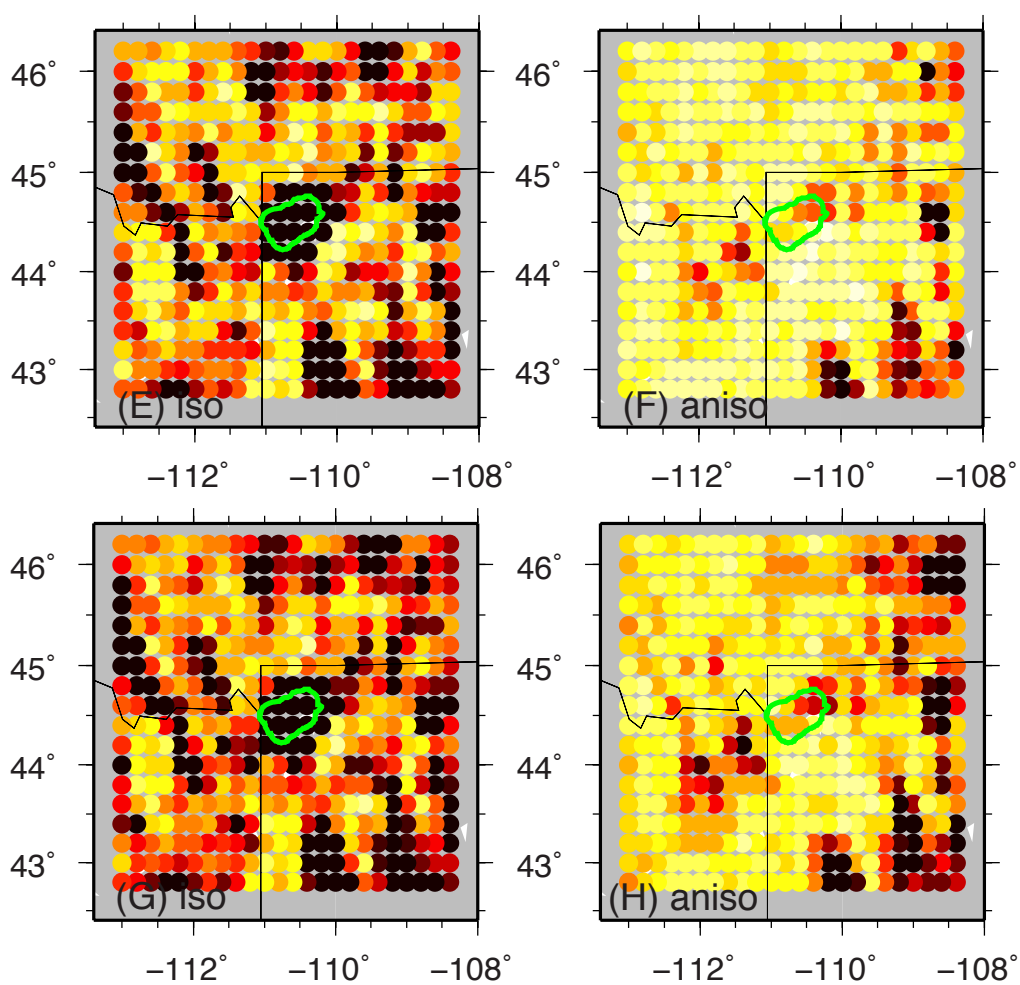


Figure DR7

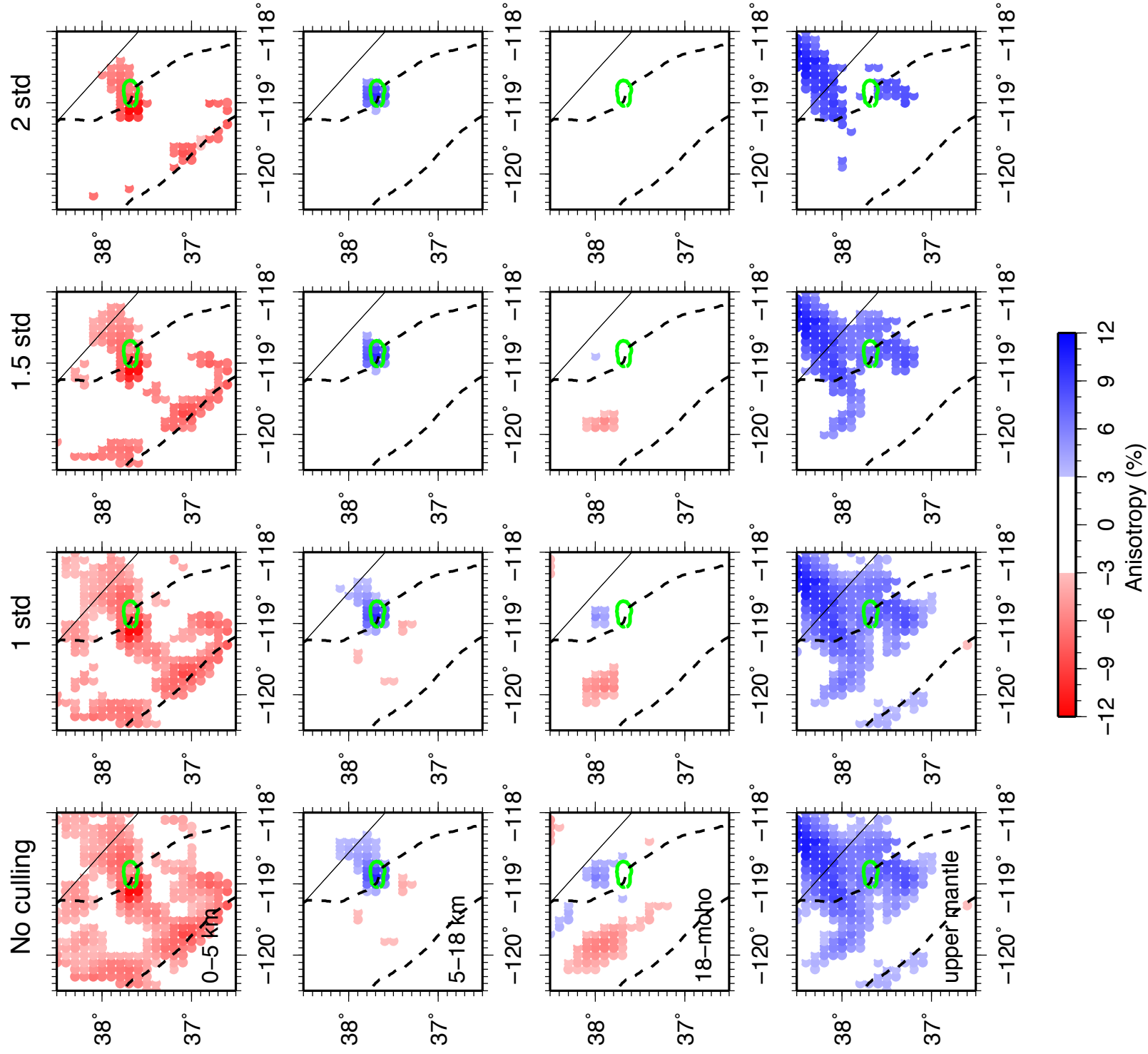


Figure DR8

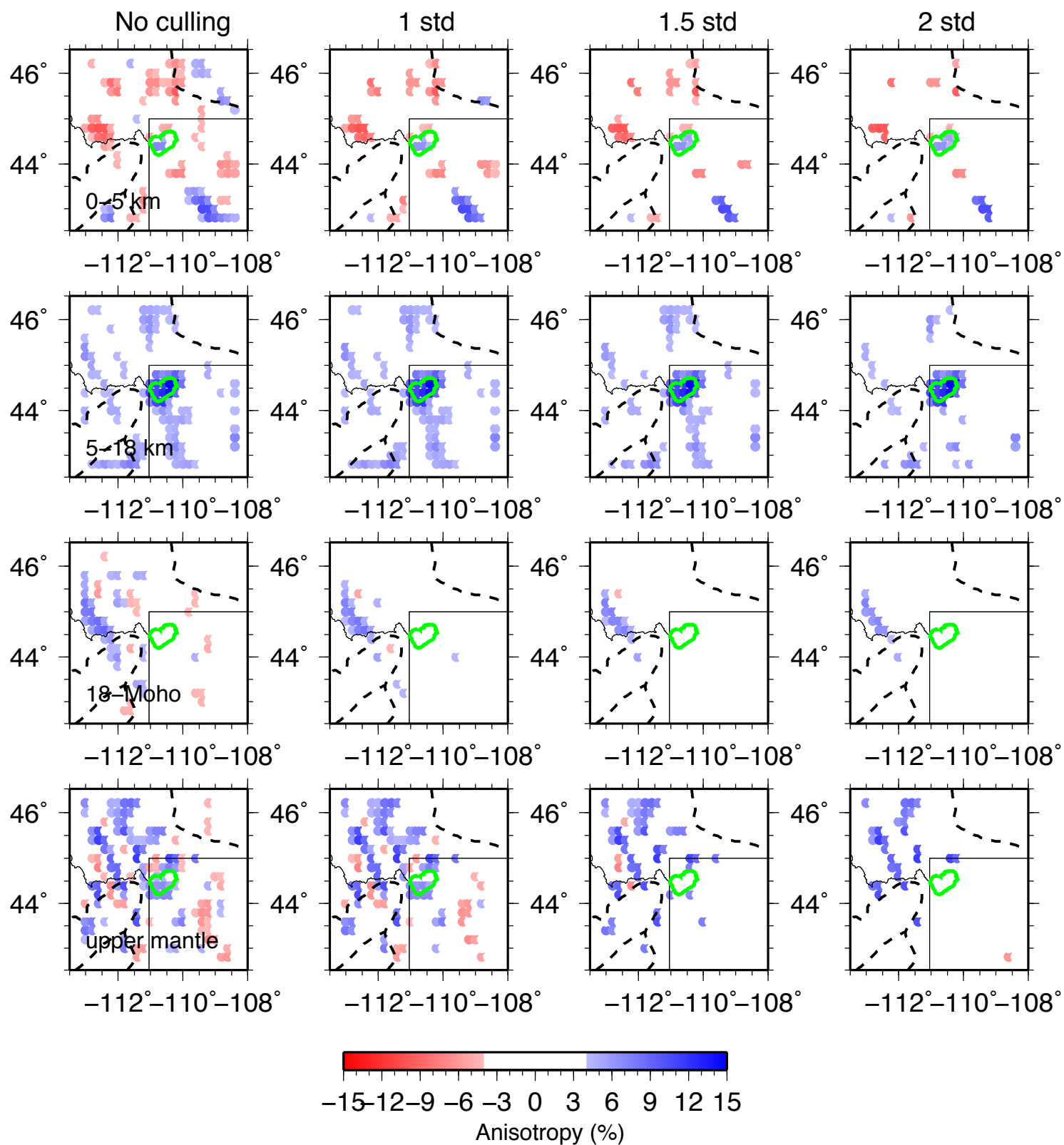


Figure DR9

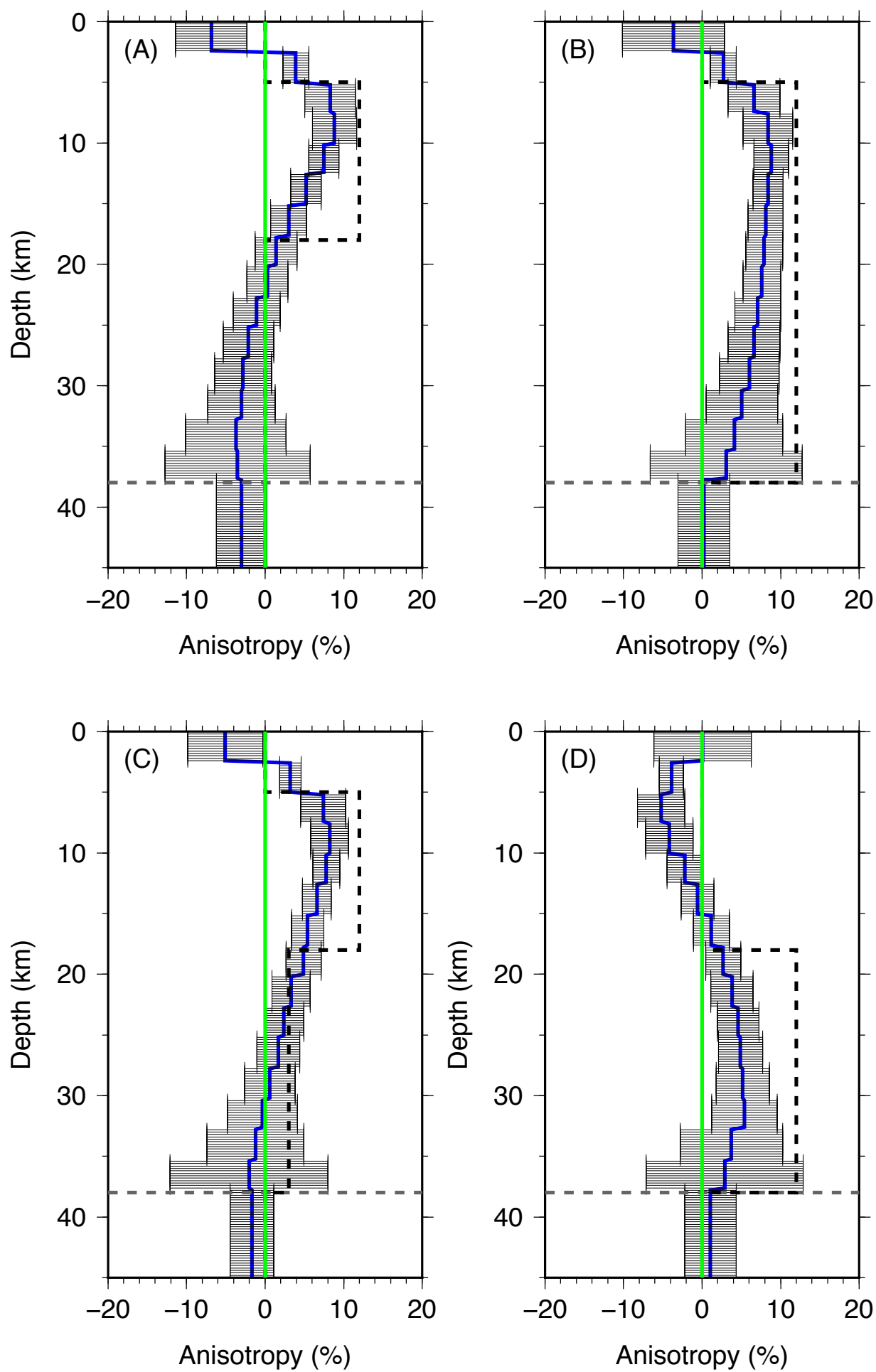
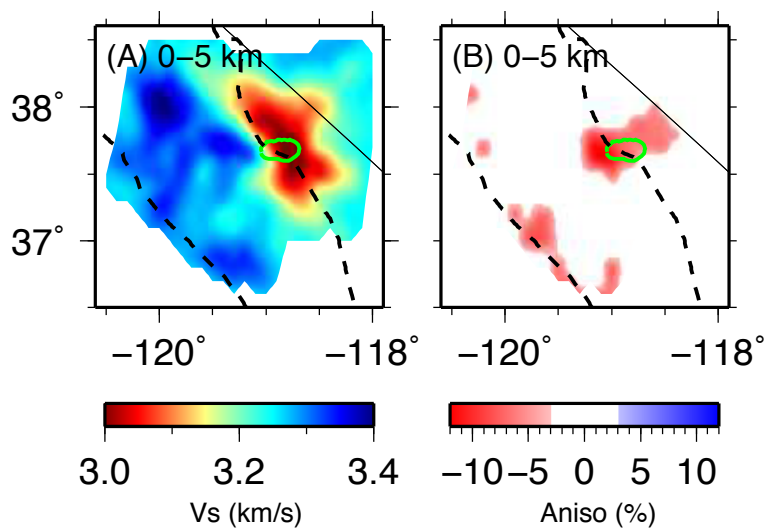


Figure DR10

Long Valley Caldera



Yellowstone

